Article
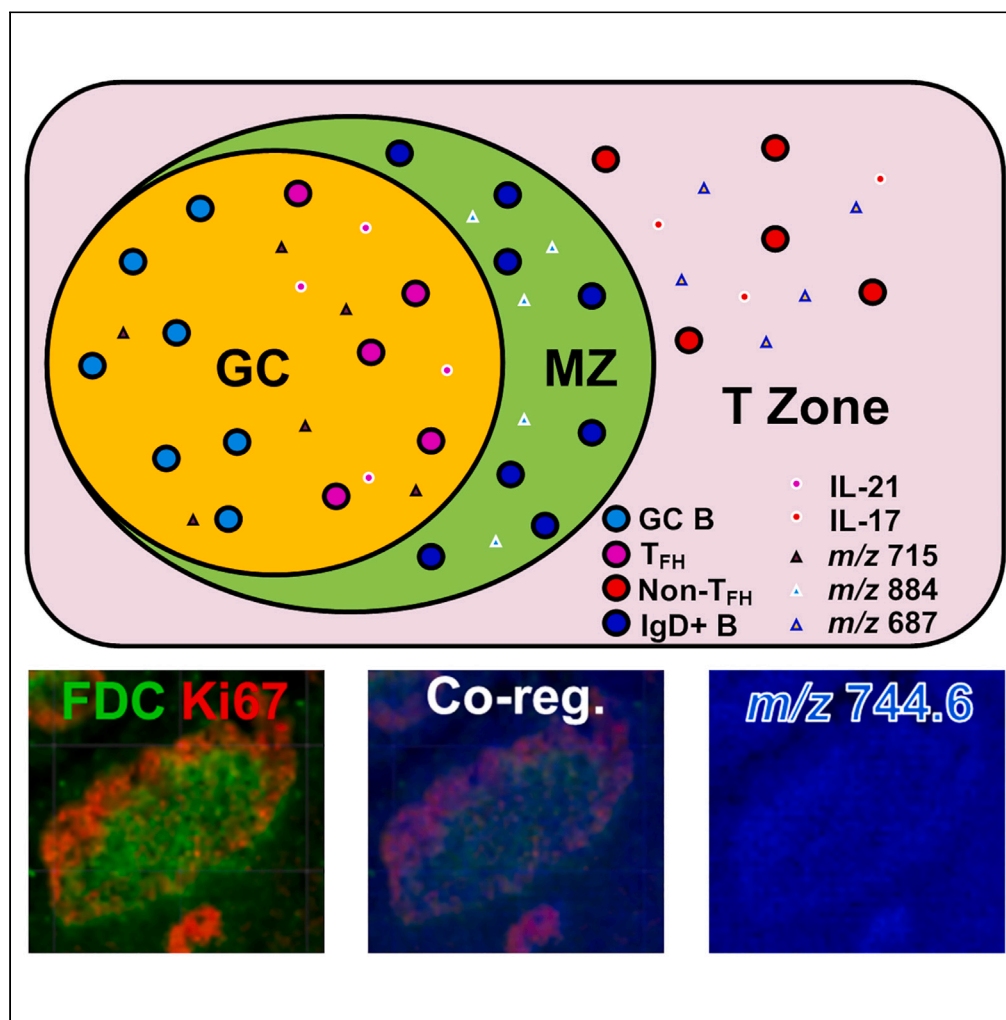
Multilevel human secondary lymphoid immune system compartmentalization revealed by complementary imaging approaches

Benjamin L. Oyler, Jeferson A. Valencia-Dávila, Eirini Moysi, ..., Amina S. Woods, Richard A. Koup, Constantinos Petrovas

konstantinos.petrovas@chuv.ch

Highlights

Multi-technique analysis and multimodal lymphoid tissue imaging pipeline developed

Lipids indicative of known tonsillar histology determined and compared to optical images

Simple co-registration of images from complementary imaging modes

Lipidomes for bulk-sorted lymphocyte phenotypes determined by MALDI-TOF MS

iScience

Article

Multilevel human secondary lymphoid immune system compartmentalization revealed by complementary imaging approaches

Benjamin L. Oyler,[1] Jeferson A. Valencia-Dávila,[1] Eirini Moysi,[1] Adam Molyvdas,[1] Kalliopi Ioannidou,[2] Kylie March,[1] David Ambrozak,[1] Laurence De Leval,[2] Giulia Fabozzi,[1] Amina S. Woods,[1] Richard A. Koup,[1] and Constantinos Petrovas[1,2,3,]*

SUMMARY

Secondary human lymphoid tissue immune reactions take place in a highly coordinated environment with compartmentalization representing a fundamental feature of this organization. *In situ* **profiling methodologies are indispensable for the understanding of this compartmentalization. Here, we propose a complementary experimental approach aiming to reveal different aspects of this process. The analysis of human tonsils, using a combination of single cell phenotypic analysis based on flow cytometry and multiplex imaging and mass spectrometry-based methodologies, revealed a compartmentalized organization at the cellular and molecular levels. More specifically, the skewed distribution of highly specialized immune cell subsets and relevant soluble mediators was accompanied by a compartmentalized localization of several lipids across different anatomical areas of the tonsillar tissue. The performance of such combinatorial experimental approaches could lead to the identification of novel** *in situ* **interactions and molecular targets for the** *in vivo* **manipulation of lymphoid organ, particularly the germinal center, immune reactions.**

INTRODUCTION

Secondary lymphoid organs (SLOs) like tonsils, lymph nodes, and spleen are anatomical sites where the development of adaptive immunity to pathogens and immunogens takes place. The organization of these organs is characterized by the presence of areas well defined by their specific stromal and immune cell phenotypes and distinct roles in the development of humoral responses.[1] These areas have been extensively investigated previously at a cellular and molecular level[2–4] using animal models and several analytical methodologies. However, the spatial organization of relevant *in situ* dynamics are less understood in humans. Follicles and germinal centers (GCs), paracortical areas, T cell zones, and medulla are major anatomical areas of lymphoid organs.[5] Trafficking of pathogens or immunogens into lymphoid organs results in the initiation of a cascade of immune reactions, ultimately leading to the development of antigen-specific B cell responses. In the T cell zone, the coordinated interaction between stromal cells (e.g., fibroblastic reticular cells, FRC), innate immunity (monocytes, macrophages, and dendritic cells), and non-differentiated CD4 T cells will start a unique reprogramming of CD4 T cells and interaction with B cells, ultimately leading to their differentiation and trafficking into the follicular areas.[6–9] Within the follicle/GC, the orchestrated spatial organization and function of highly differentiated immune cell populations and stromal cells (e.g., Follicular Dendritic Cells, FDCs) will lead to the development of antigen-specific B cell responses.[10] Specifically, the GC is characterized by two distinct areas[11]—the Light Zone (LZ), where the interaction between follicular helper CD4 T cells (TFH), GC B cells, antigen, and FDC takes place;[12,13] and the Dark Zone (DZ), wherein the division and further maturation of B cells occurs.[14] The outcome of the B cell responses is critically dependent on the quality and specificity of the "help" received from T_{FH}.[15]

Compartmentalization of the relevant immune reactions and players is a critical component for their coordinated function. This compartmentalization could facilitate the ordered, multiphase development of these immune interactions while likely providing checkpoints for their regulation and the suppression of unwanted immune reactivity like autoimmunity. The relative accessibility, compared to other human

[1]Tissue Analysis Core, Immunology Laboratory, Vaccine Research Center, NIAID, NIH, Bethesda, MD, USA

[2]Department of Laboratory Medicine and Pathology, Institute of Pathology, Lausanne University Hospital and Lausanne University, Lausanne, Switzerland

[3]Lead contact

*Correspondence: konstantinos.petrovas@chuv.ch

https://doi.org/10.1016/j.isci.2023.107261

lymphoid organs, the abundance of relevant immune cell types, and the well-preserved anatomical areas (e.g., GCs) makes reactive human tonsils a prototype lymphoid organ for the study of follicular immune dynamics with respect to the local microenvironment.

To address the need for a robust multimodal analysis pipeline in lymphoid tissue biology, we have applied complementary single cell analysis and quantitative imaging methodologies to further characterize the organization of tonsillar anatomy both at cellular and molecular levels. Previous research to address this need is sparse. There have been several approaches to multimodal imaging of tonsillar tissue using a limited number of cell phenotype probes for T and B lymphocytes.[16,17] One of these approaches was performed for the purpose of identifying tumor infiltrating lymphocytes which is quite different than the purpose of our research.[17] Another approach gaining traction uses dual labeled antibody probes to perform immunohistochemistry.[18] This is very innovative and attractive but requires additional cost and method optimization. Flow cytometry represents a reference fluorescence-based technique for phenotyping of cells in solution. Despite its power, flow cytometry cannot provide any information for the spatial positioning of analyzed tissue-derived cells. On the other hand, fluorescence-based multiplex imaging assays (mIF), combined with a quantitative pipeline like HistoCytometry, visualize the positioning of cell subsets within a given tissue and enumerate the cell phenotypes within a given tissue segment. Given the availability of appropriate probes, the "targets" for mIF assays are limited to protein, mRNA, and DNA molecules. Mass spectrometry imaging (MSI) is an alternative tissue imaging technique wherein ionizable compounds are desorbed from the tissue surface and detected in a mass spectrometer to generate images of these compounds. Of interest, ions of different nature (proteins, peptides, lipids, etc.) can be imaged by MSI in a targeted or non-targeted, unsupervised mode. Furthermore, dedicating part of a given tissue for sorting of relevant tissue lymphocyte subsets and their analysis with mass spectrometry can reveal molecular differences between cell phenotypes and cross-validate MSI-generated data from the same tissue. Combination of the aforementioned types of data can provide a comprehensive experimental approach for the study of the spatial organization within human lymphoid organs, especially in the context of disease and/or treatment paradigms. Furthermore, we propose a novel approach for the investigation of tissue organization using lipid signatures. Addition of these data to the cellular and imaging data for preclinical and clinical studies will enable a novel systems-level approach to immunology and virology research.
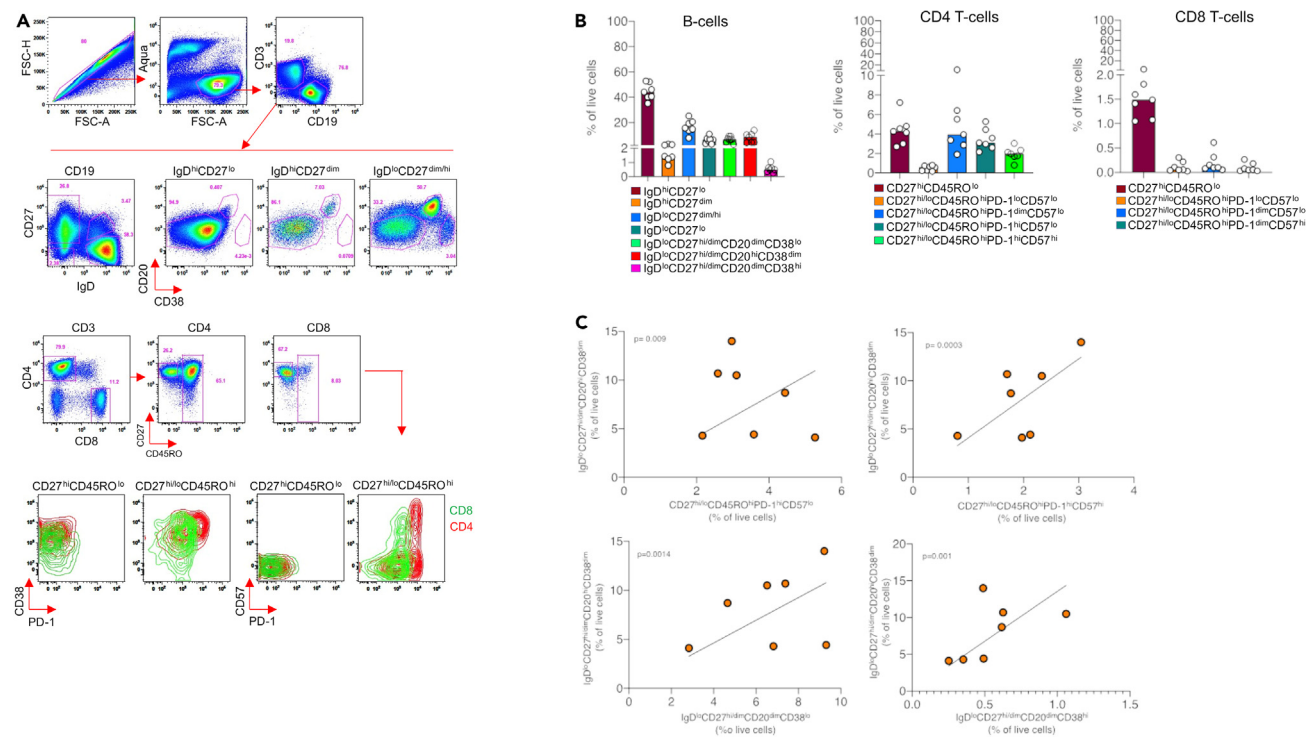
RESULTS

Assessing the tonsillar cellular composition

We started our analysis by applying a multiparametric flow cytometry assay focusing on the immune cell types (T and B cells) that constitute the vast majority of non-adherent cells in human tonsils (Figure 1A). B cells ($CD19^{hi}$) were further characterized by their expression of CD27, IgD, CD20 and CD38. An enrichment of the $CD20^{hi}CD38^{dim}$ subset (a phenotype compatible with GC localization[19]) was found specifically in the $IgD^{lo}CD27^{dim/hi}$ memory B cell compartment (Figure 1A). CD4 positive cells, which constitute the majority of CD3 T cells, present a subset expressing the unique phenotype $PD-1^{hi}CD57^{hi/low}$ (T_{FH})[20] (Figure 1A). A similar representation of memory B cell subsets was found whereas plasma cells ($CD19^{hi}CD27^{hi}IgD^{lo}$ $CD20^{dim}CD38^{hi}$) was the subset with the lower frequency (Figure 1B). Cumulative data analysis showed a relatively high frequency of T_{FH} cells whereas the majority of CD8 T cells express a naive ($CD27^{hi}CD45RO^{lo}$) phenotype (Figure 1B). A significant correlation was found between $CD19^{hi}CD27^{hi/dim}IgD^{lo}CD20^{hi}CD38^{dim}$ (most likely resembling GC B cells) and (1) T_{FH} subsets, (2) $CD19^{hi}CD27^{hi/dim}IgD^{lo}CD20^{dim}CD38^{lo}$ (most likely representing memory non-GC B cells), and (3) plasma cells (Figure 1C). A mutual regulation between T_{FH} and GC B cells has been previously proposed.[6] Our data indicate that such regulation takes place during the development of the tonsillar follicular/GC reactions.

Skewed distribution of immune cell subsets and mediators of cell-to-cell communication among tonsillar areas

Despite the quantitative characterization of tonsillar cells by flow cytometry, this type of analysis does not provide any direct information regarding the localization of relevant cell subsets. Therefore, we sought to develop mIF assays to address the localization of relevant cells and soluble mediators like the cytokine IL17 and chemokine CXCL13. Annotation of relevant tonsillar tissue compartments (i.e., Mantle Zone-MZ and GC) is shown in Figure 2A. Our confocal imaging assay allows for the simultaneous detection of (1) B cell subsets, with respect to the expression of IgD, CD20, and Ki67, (2) T_{FH} cell subsets, based on the expression of PD-1 and CD57, and (3) CD8 T cells and macrophages ($CD68^{hi}$) (Figure 2B). The quantitative analysis of the obtained imaging data was carried out using the HistoCytometry pipeline.[21,22] The gating scheme for

Figure 1. Assessment of the tonsillar cellular composition with multiparametric flow cytometry

(A) The gating scheme for the flow cytometry analysis of relevant cell subsets is shown (upper panel). The relative expression (intensity) of CD38, PD1 and CD57 in tonsillar CD4 (red) and CD8 (green) subsets is shown (lower panel). The overlay of corresponding 2D flow cytometry plots visualizes the different level of expression between the two T cell subsets with T$_{FH}$ cells expressing the highest level of PD1.

(B) Bar graphs showing accumulated data regarding the relative frequency of B, CD4 and CD8 subsets in tonsils (n = 7) analyzed.

(C) Significant correlation between GC B cells and TFH subsets and GC B cells and plasma cells. Linear regression was used for the analysis.

the identification of specific cell populations with respect to their area localization is shown in Figure S1. Our analysis showed a highly skewed distribution of CD4, CD8 and B cell subsets across different follicular areas (Extrafollicular Area, MZ and GC) (Figure 2B). Supporting the phenotypic characterization of the aforementioned B cell subsets (Figure 1A), CD20 expression was lower in the MZ (IgD positive area) and higher in the GC, particularly the LZ, in line with previous data.[19,20] Furthermore, the PD-1^{hi}CD57^{hi} CD4 T$_{FH}$ cells were found almost exclusively in the follicular area, specifically the GC (Figure 2B), in agreement with our recent data.[20] On the other hand, CD8 T cells were highly excluded from the follicular areas while most CD68^{hi} macrophages were found in follicular areas (Figure 2C). A significant correlation was found between GC (CD20^{hi}Ki67^{hi}) B cells and PD-1^{hi}CD57^{hi} CD4 T$_{FH}$ cells (Figure 2C) in line with our flow cytometry data. The application of a second multiplex imaging assay revealed the localization of the FDC network within GCs, associated with an abundant expression of CXCL13 (Figure 2D), the main driving force for the trafficking of CD4 T cells and B cells toward the GC.[23] On the other hand, IL17 expression was found almost exclusively in the Extrafollicular Area (Figure 2D), in line with our previously reported data related to the capacity of individual CD4 T cell subsets for IL17 secretion.[24] Contrary to CD68^{hi} macrophages, CD14^{hi} monocytes were found to populate extrafollicular areas (Figure 2D). Therefore, in addition to the compartmentalization of immune cell types and soluble factors across the tonsillar areas, our data reveal the 'exclusion' of specific cells (e.g., CD8, CD14) from tonsillar GCs.

Compartmentalized localization of tonsillar lipids

Then, we sought to investigate the *in situ* distribution/localization of lipids, which represent critical components for the structure of cellular membranes, intracellular signaling, and communication between cells (chemo-attractants).[25] The general scheme of the experimental pipeline for lipid imaging using MSI and subsequent ion identification by MS/MS is shown in Figure S2A. An on-tissue, space-directed MS/MS approach was used to reduce combined fragmentation of isobars (ions with different chemical structures but the same nominal mass) which may be found overlapping in the average mass spectrum but are
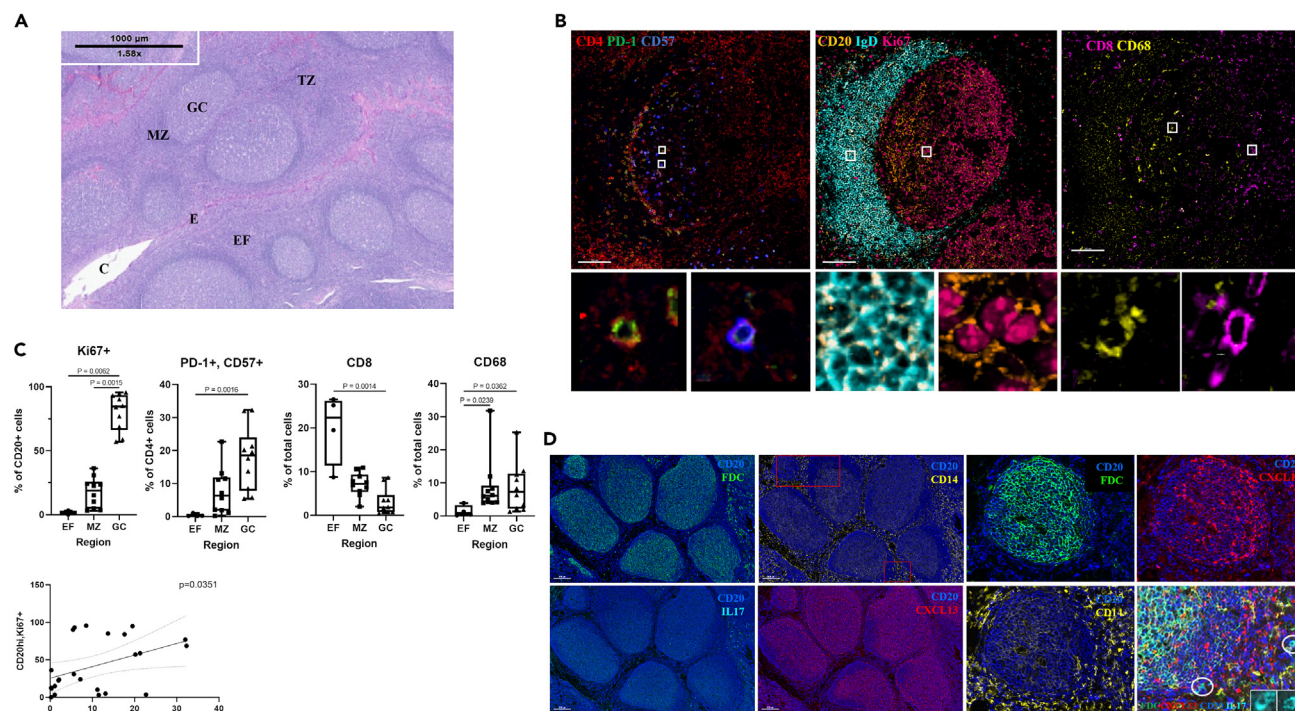
Figure 2. Compartmentalization of tonsillar cell types and soluble mediators revealed by multiplex imaging analysis

(A) Representative hematoxylin and eosin (H&E) stained human tonsil section. Relevant anatomical segments are labeled for tonsillar crypt (C), germinal center (GC), mantle zone (MZ), crypt epithelium (E), T cell zone (TZ) and extrafollicular area (EF).

(B) Representative multiplex confocal images showing the distribution of B, CD4 and CD8 cell subsets in a follicular area and adjacent 'T cell area'. Zoomed areas (white boxes) are also shown for the visualization of the expression of relevant biomarkers on individual cells. Scale bars top row are 100 μm.

(C) Bar graphs showing the relative expression (as frequency of the corresponding parental population) of Ki67$^+$ B cells and PD-1$^+$CD57$^+$ CD4 T cells as well as the frequency (of total cells) of CD8 and CD68 subsets in different tonsillar areas (EF = extrafollicular, MZ = mantle zone, GC = germinal center) (upper panel), Kruskal-Wallis ($\pm$ SEM) statistic test used significant differences notated. The correlation between Ki67$^+$ GC B cells and PD-1$^+$CD57$^+$ CD4 T$_{FH}$ cells is shown (lower panel), Simple linear regression statistical test used.

(D) Representative multispectral images showing the distribution of FDCs (green), CD14 (yellow), CXCL13 (red) and IL17 (cyan) with respect to the follicular areas (CD20, blue) in one tonsil. Inserts are showing the expression of IL17 in zoomed areas (white circles). Scale bars are 200 μm.

distributed differently throughout the tissue. Briefly, collisional activation and subsequent spontaneous decomposition was performed in the collision region of the TOF/TOF after focusing the laser in a single 20 μm beam on the region where the compound of interest was shown to reside in the sample. We started our investigation by analyzing lipids with MSI in positive mode, using DHB matrix, data acquisition at 20 μm lateral resolution (Figure S2B), and data normalization using root-mean-square (RMS) correction (Figure S2C). The average single stage mass spectrum across the entire imaged tissue (inset) and a zoomed region from *m/z* 700 to 750 to indicate the ions used for further analysis, are shown (Figure 3A). In total, 74 common monoisotopic *m/z* peaks were detected when the mass spectrum was averaged across the entire tissue and compared between different tonsillar specimens (N = 3). Twenty of these peaks were found to be localized to the tissue segment designated as the follicular area. These peaks, identified as lipids, did not always display a similar tissue distribution but in all cases were more abundant in the follicular area than in other tissue regions (Figure S3). An exhaustive characterization of all detected ions, with treatment of each spectrum separately, may be necessary for discovery of novel biological phenomena in the future. Most of the abundant peaks in the spectrum correspond to protonated ([M + H]$^+$) phosphatidylcholines (PCs), with less frequent peaks corresponding to sodiated ([M+Na]$^+$) diacylglycerols (DAGs), protonated sphingomyelins (SMs), and lyso-lipids (Figure S3). SMs are observed with the same ionization characteristics as PCs because of their identical phosphocholine head group; therefore, they are not easily differentiated in positive mode MS. Using the nitrogen rule,[26] inferences were made regarding the identities of these ions (i.e., odd mass ions were inferred to be primarily from SM monoisotopic ions and even mass ions were inferred to be primarily from PC monoisotopic ions). Collisional activation and dissociation of these ions suggests that some include isobaric isotopic peaks from other species. We focused on three
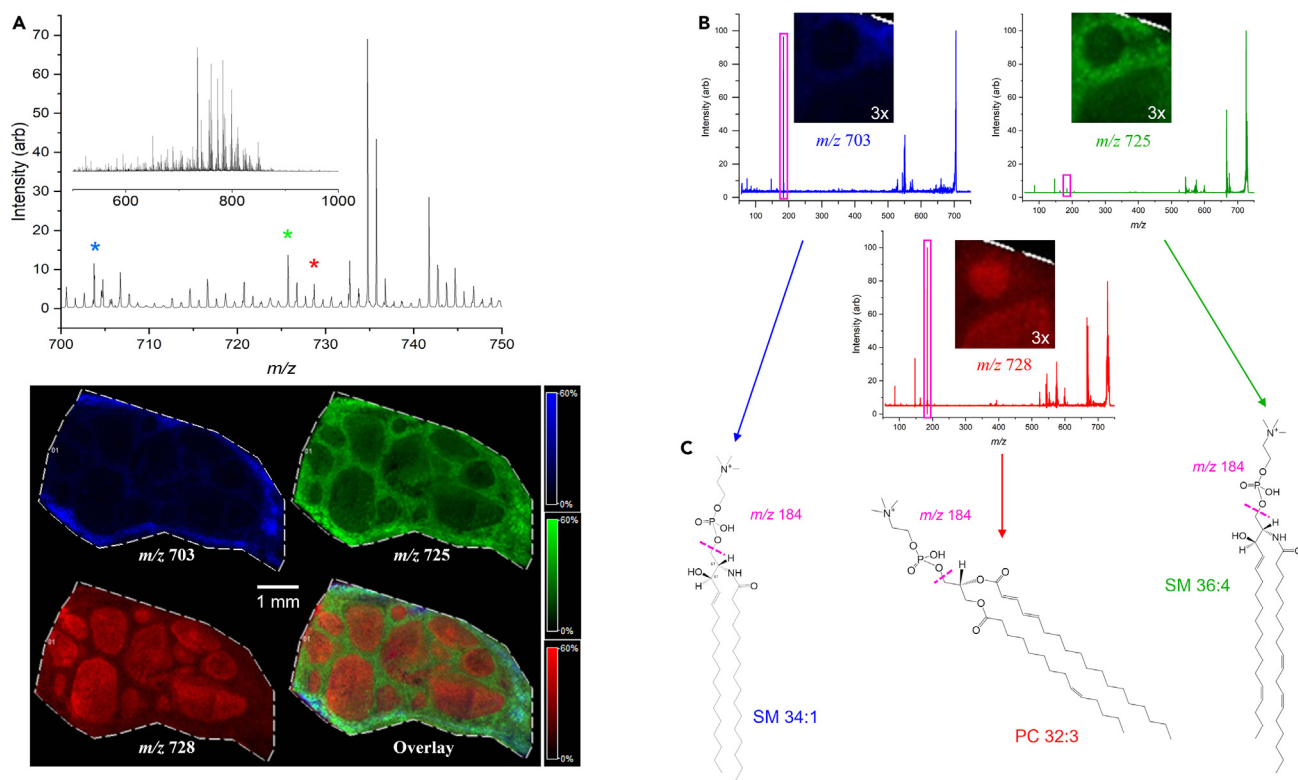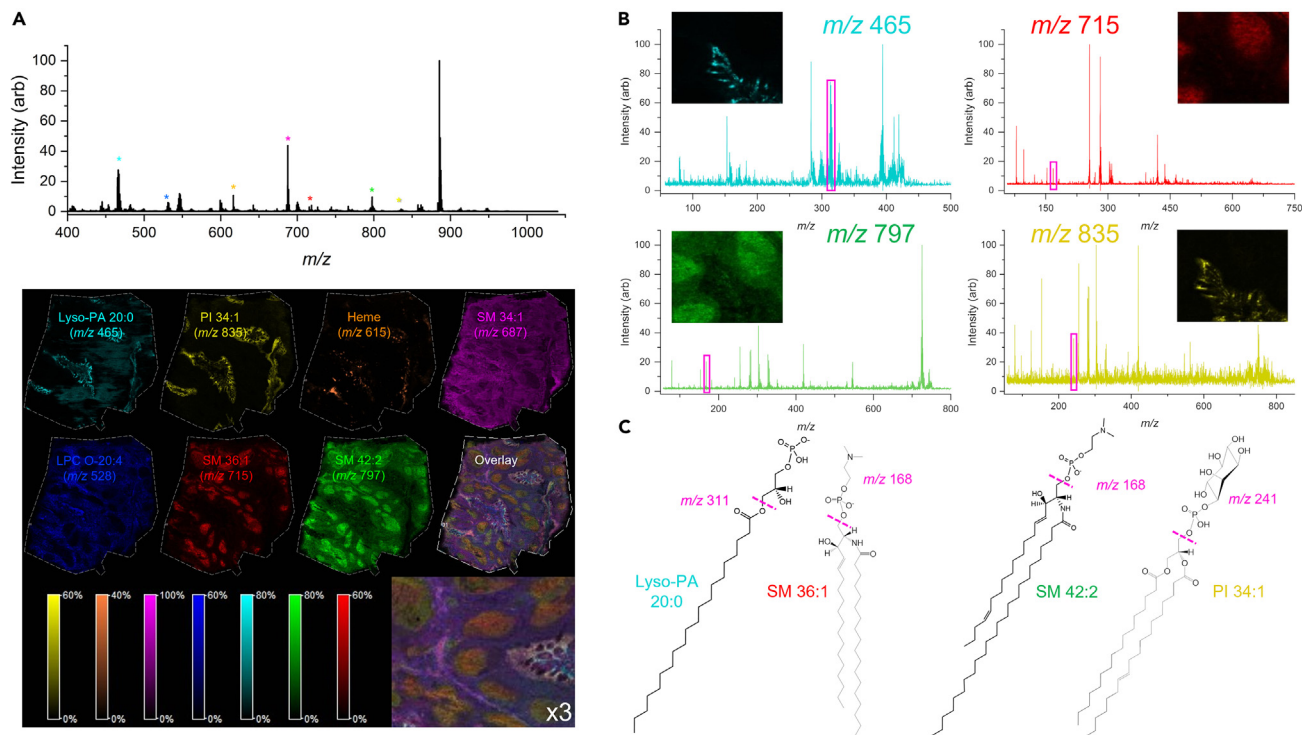
Figure 3. Differential localization of lipids across tonsillar areas revealed by positive ion MSI

(A–C) Average positive ion mode single stage TOF mass spectrum showing lipids detected over the mass range *m/z* 500–1000 (A, top inset) using DHB as MALDI matrix. Lipid ions used to create 20 μm lateral resolution images (A, bottom) are indicated in the region *m/z* 700–750 with asterisks corresponding to the colors used to generate images (A, top). Tandem mass spectra for each of the three lipids (B) were acquired to determine lipid class. Magenta boxes indicate the characteristic phosphocholine ion at *m/z* 184 determining these ions as either SMs or PCs. 3× zoom regions of the images around two tonsillar follicles are shown for clarity. Putative structure identifications using precursor ion mass and head group product ion mass are shown for each of the three ions (C). Odd mass precursor ions were inferred to be from SMs and even mass precursor ions were inferred to be from PCs. Lipid isomers may be present in the sample and acyl chain double bond positions indicated in the figure are not determinable using the positive ion mode method applied.

ions (*m/z* 703, 725, and 728) for further analysis. The localization of these ions across the entire tissue resembles tonsillar epithelium or connective tissue, extrafollicular, and follicular areas, respectively (Figure 3A), and they were putatively identified as SM 34:1, SM 36:4, and PC 32:3 using precursor ion mass and product ion spectra from the same instrument as was used to acquire images. Their tandem mass spectra (LIFT MS/MS) and respective zoomed images to better visualize the tissue micro-anatomy are shown in Figure 3B. The magenta boxes indicate the ion channel at *m/z* 184 (phosphocholine ion), identifying these ions as either PCs or SMs. The corresponding structure of these three lipids is also shown (Figure 3C). The structure identifications are putative as there could be several isomers or isobars isolated and fragmented in the tandem mass spectra. The major lipid classes in the tandem mass spectra are defined by the polar lipid head group product ions indicated.

Next, negative mode MSI was performed using DAN matrix and imaging at 20 μm lateral resolution (Figure S4A). In total, 80 common monoisotopic *m/z* peaks were detected when the mass spectrum was averaged across the entire tissue and compared between patient specimens (N = 3). Twenty-four of these peaks were found to be localized to the tissue segment designated as the follicular area (Figure S4B). We further focused our analysis on seven ions, putatively identified as lyso-PA 20:0, PI 34:1, heme, SM 34:1, LPC O-20:4, SM 36:1, and SM 42:2 (Figure 4A, upper panel). Their localization across the imaged tissue is shown (Figure 4A, lower panel). The tandem mass spectra (LIFT MS/MS) for four of the ions imaged (Figure 4B), and their basic structure elucidation scheme (Figure 4C) are shown as well. The magenta boxes (Figure 4B) indicate the ion channels corresponding to the glycerophospholipid head group ions used to identify SM 36:1, SM 42:2, and PI 34:1, and the fatty acyl carboxylate anion from lyso-PA 20:0. Figure 4C shows representative lipid structures for each of the precursor ions in Figure 4B. These are putative identifications

Figure 4. Differential localization of lipids across tonsillar areas revealed by negative ion MSI

(A) Average negative ion mode single stage mass spectrum in the mass range m/z 400–1050 using DAN as MALDI matrix (A, top). Ions used to generate 20 μm lateral resolution images in the bottom panel are indicated with asterisks in their corresponding colors in the mass spectrum. Extracted ion images (EII) for each of the lipid ions indicated are shown (A, bottom) along with an overlay of the seven ions chosen to create the histological image.

(B) Tandem mass spectra for four of the ions chosen to create the tissue image are shown with magenta boxes indicating the polar lipid head group product ion used to identify the lipid class. In the region m/z ~200–315, fatty acyl carboxylate anions can be seen in the negative ion mode tandem mass spectrum. While the positions of acyl chain double bonds cannot be determined using this method, SMs can be differentiated from PCs based on their lack of acyl chain product ions in contrast to positive ion mode where they cannot be differentiated.

(C) Basic structure elucidation schemes with representative structures for the ions imaged are shown. The lysophosphatidic acid is putatively identified by its fatty acyl carboxylate product anion at m/z 311. The phosphocholine product ions from PCs and SMs in negative ion mode always lose a methyl group, indicated by the change in mass from m/z 184 to m/z 168. The phosphoinositol head group mass in negative ion mode is m/z 241, along with other small indicative phosphoinositol fragments.

because there could be several lipid isomers or isobaric compounds isolated and fragmented in the tandem MS experiments. However, the major lipid class was positively identified by the head group product ion. Collectively, our data demonstrate that tonsillar areas are characterized by distinct positioning of many lipid molecules, possibly contributing to the structural and functional compartmentalization of this lymphoid organ. Specifically, m/z 465, 835, and 615 seem to be localized to the capillaries and other epithelium-rich areas, while m/z 715 and 797 are in higher abundance in the lymphoid tissue (specifically the GC for m/z 715).

Computational analysis of lipid compartmentalization

Computational tissue segmentation, for both positive and negative ion modes, was performed using the SCiLS Lab Pro segmentation module. Two different m/z ranges were used to automatically segment the tissue in negative ion mode. Use of the 300–1100 m/z range resulted in poor tissue segmentation while the 400–1100 m/z range provided a segmentation resembling the tissue micro-anatomy observed by the corresponding imaging of tissue using a nuclear marker (Figure S5A). It is likely that extending the mass range below m/z 400 included matrix ions in the segmentation, a confounding factor for the segmentation algorithm. Automatically generated tissue segments were further assigned as tissue regions in the software. The three tissue segments assigned to the tonsillar follicle, extrafollicular area, and tonsillar crypt were used for further processing and statistics. Receiver operating characteristic (ROC) curves were used for the validation of a given ion to discriminate between the tonsillar segments (Figure 5A). An ion specific
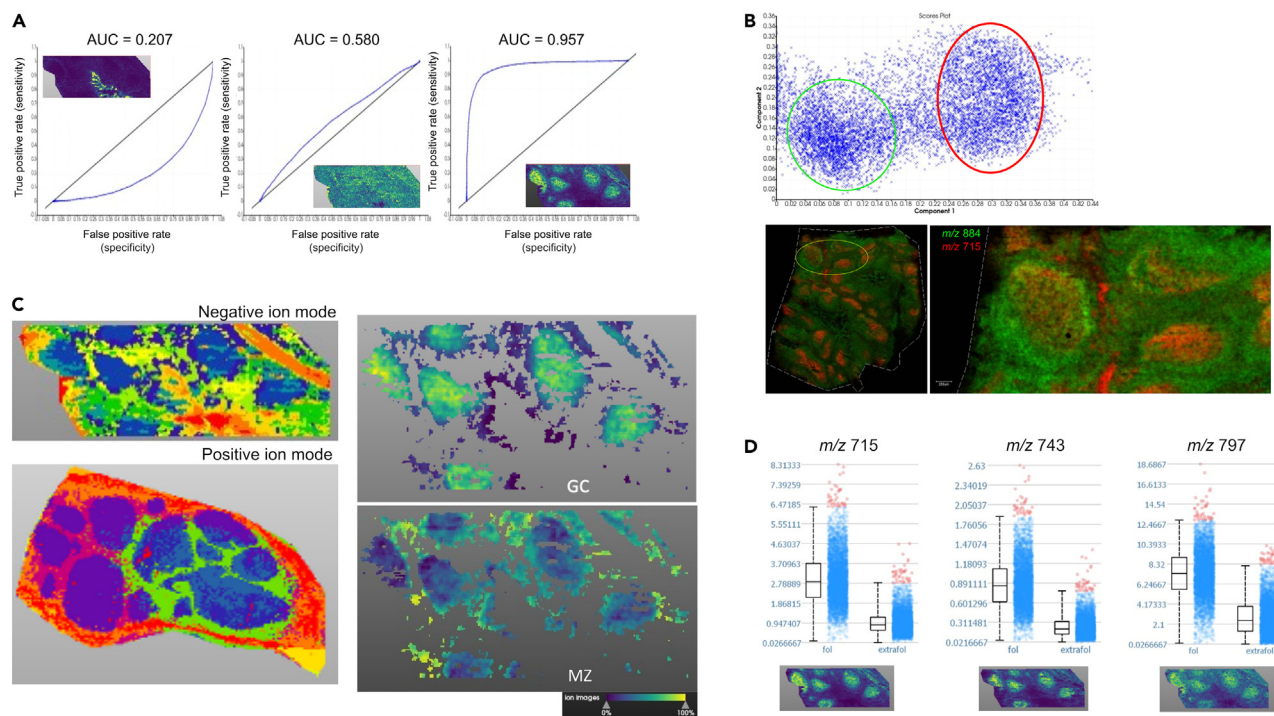
Figure 5. Computational analysis of lipid ions' distribution in tonsillar regions of interest

(A) Receiver operating characteristic (ROC) curves for three ions in negative ion mode when comparing the specificity of each ion for the follicular area versus the extrafollicular area. Area under the curve (AUC) for an ion specific to the tonsillar crypt/epithelium was 0.207, indicating it is not specific to the follicle. AUC for an ion found relatively evenly distributed across the tissue was 0.580, indicating that it is found in the follicle but not specific to that area versus the extrafollicular area. AUC for an ion specific to the follicle was 0.957, indicating its ability to differentiate the follicle from the extrafollicular area. Images of the three ions used to generate the ROC curves are shown as insets.

(B) Probabilistic latent semantic analysis (pLSA) using a model with five components showing a bimodal distribution of data points in the region defined as the follicle (top). Circles were drawn around the data points for emphasis. Two ions, m/z 715 and m/z 884, are representative of two regions of the follicle computationally derived and shown for analysis clarification (bottom).

(C) Computational segmentation of tonsillar tissue in negative and positive ion modes using all features in each individual mass spectrum from the imaging experiments (left panels) and computational regeneration of the data from the pLSA indicating the region defined as the follicle could be further divided into two distinct regions (right panels) inferred to be the germinal center (GC) and the mantle zone (MZ).

(D) Three ions (m/z 715, 743, and 797) found to be specific to the follicle versus the extrafollicular space, but demonstrating unique tissue localization images (bottom) indicating that these lipids are compartmentalized slightly differently in the tissue. Box and whiskers plots show that in all cases the median intensity values of these ions are higher (p < 0.002 for all three ions) in the follicle than in the extrafollicular space.

for the crypt and an ion that uniformly distributed across the tissue gave AUC values of 0.207 and 0.580, respectively, while a follicle-specific ion gave a value of 0.957, associated with a distinct distribution pattern primarily within the follicle (Figure 5A). An AUC value of 1.000 in this analysis is considered ideally specific and sensitive to distinguish one segment from the other. A probabilistic latent semantic analysis (pLSA) was performed to identify lipids that could contribute to the differential imaging profiles across follicular sub-areas. Similar to a principal component analysis, a pLSA creates "components" or vectors of the dataset with discriminatory power and plots data groups on axes created from those components. Discriminatory power of each individual ion and its contribution to the component can be extracted and used for biomarker discovery, if needed. A bimodal distribution of ions was observed in the pLSA (Figure 5B, upper panel), indicating a differential expression of lipids among follicular areas, likely GCs and MZs in this case (Figure 5B, lower panel). Representative tissue segmentation images are shown in both positive and negative ion modes for a visual reference of the segmentation performance (Figure 5C, left panels). The tissue segmentation maps were generated with the identified regions arbitrarily given different colors for contrast. The regenerated images using the negative ion mode pLSA data points from each cluster in the region defined as the follicle are also shown in Figure 5C (right panels). Tissue segmentation maps were generated automatically in SCiLS Lab Pro using all the features (m/z channels) detected in the imaging run, pixel-by-pixel. Pixels with similar features and relative abundances of those features were grouped
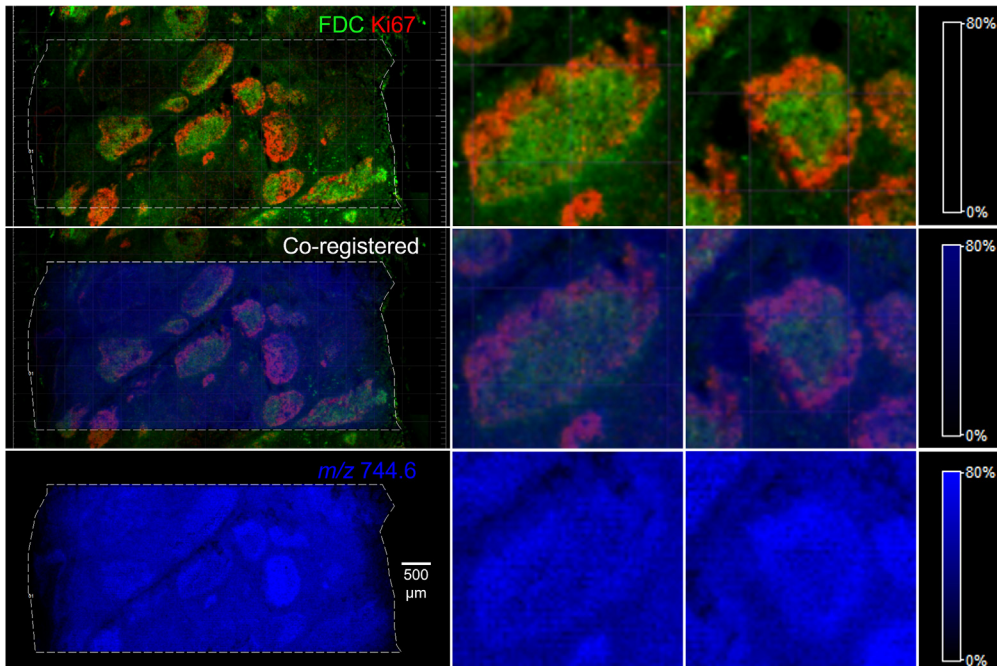
Figure 6. Co-registration of mIF- and MSI-generated images reveals differential localization of lipid ions with respect to identified cell types *in situ*

Top row: confocal image of follicular dendritic cells (FDCs) and Ki67 + B cells, indicating follicular germinal centers (GC). Zoomed images around two GCs are shown as well. Middle row: co-registered mass spectrometry and confocal images showing a lipid at *m/z* 744.6 localized to the GC and in higher intensity in the Ki67+ regions. Bottom row: negative mode extracted ion (*m/z* 744.6) mass spectrometry image with 20 μm lateral resolution. Color index bars representing relative intensity of *m/z* 744.6 in each image are displayed to the right of each row.

together as segments. Some segments were then grouped together manually to represent the known tonsillar tissue architecture.

We further explored the distribution of three ions (*m/z* 715, 743, and 797) preferentially localized to the follicle relative to the extrafollicular area. Their relative quantification revealed a significantly ($p < 0.002$ for all 3 ions) higher median presence in the follicle than in the Extrafollicular Area, in two different patient specimens (Figures 5D and S5B), which is a computational result consistent with what is observed with the eyes in the corresponding images (Figures 5D and S5B). Therefore, the shown computational analysis represents a robust pipeline for the relative quantitative analysis of a given lipid with respect to its tissue localization.

MSI and mIF co-registration and interpretation

A strategy for multimodal imaging of one tissue section was employed using negative ion mode lipid MSI at 20 μm lateral resolution followed by staining with relevant antibodies and subsequent imaging using a laser scanning confocal system. Frozen tissues were used and experimental conditions were optimized for the acquisition of confocal images following the application of appropriate matrix and MSI. Confocal microscopy images were processed with Imaris software to generate .tif images which were then imported to FlexImaging. The onboard co-register image tool was used to align the confocal image with the optical image from the scanned slide (Figure 6). Since we used the same tissue section for both MSI and confocal imaging, reference points were relatively easy to find in most cases. Staining for FDC and Ki67 identifies tonsillar GCs, particularly the Light Zone (enriched for FDC) and the Dark Zone (enriched for proliferating, presumably B, cells) areas (Figure 6, upper panel). The spatially co-registered mIF and MSI image (Figure 6, middle panel) showed that *m/z* 744.6 was mainly localized to the Ki67-rich area of the GC, indicating its possible specificity for proliferating B cells. The extracted ion image of *m/z* 744.6 alone (Figure 6, bottom panel) is shown for clarity. Our approach allows the co-localization of relevant tonsillar cells with any identified ions of interest, considerably increasing our ability for tissue analysis.
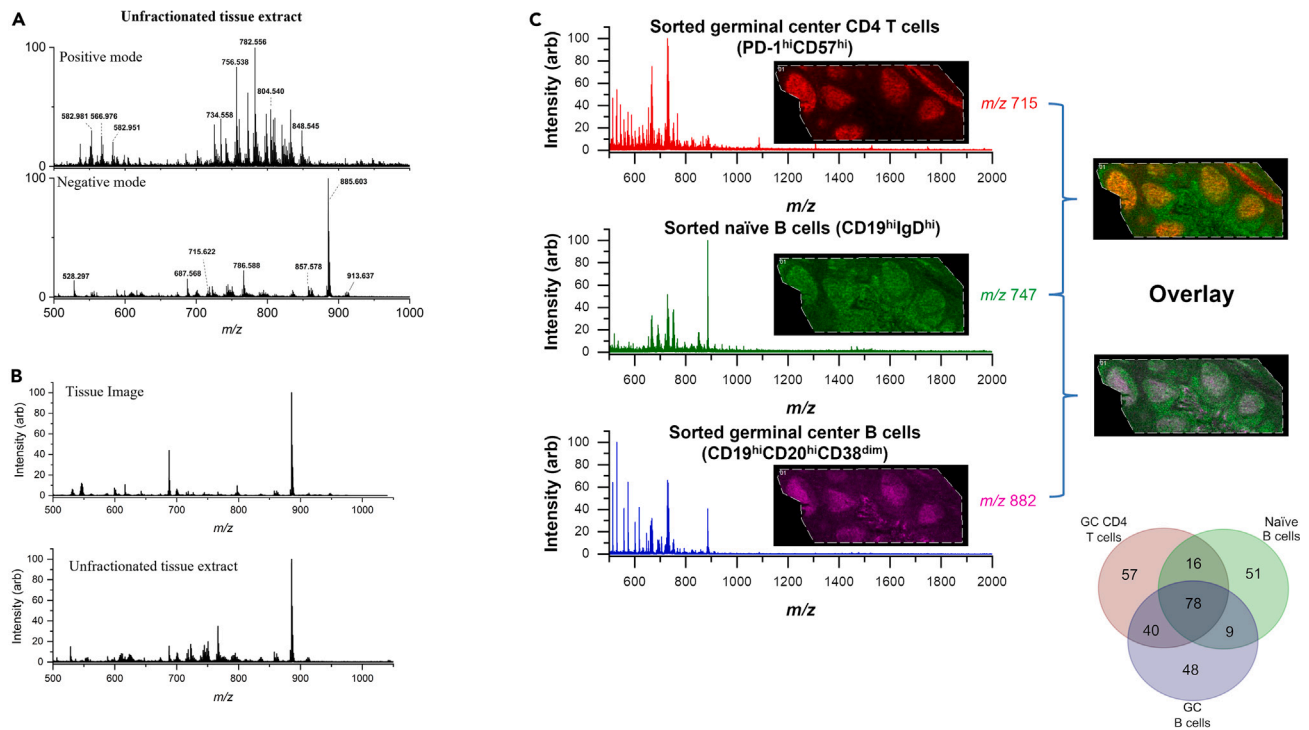
Figure 7. Commonly expressed lipids in follicular areas and related cells revealed by mass spectrometry analysis

(A) Broadband single stage mass spectra in positive (top) and negative (bottom) ion modes for unfractionated tonsil tissue extract using DHB and 9-AA as matrices in positive and negative ion modes, respectively. Small pieces of tissue were dissected from a frozen tonsil and extracted using a total lipid extraction method.

(B) Average broadband single stage mass spectra acquired in negative ion mode from a tissue image (top) versus an unfractionated tissue extract (bottom). While more features were detected in the tissue extract, and some with slightly different relative abundances, the major features and their relative abundances in the mass spectra were strikingly similar.

(C) Mass spectra shown are broadband negative ion mode spectra from the sorted tonsillar cell subsets: GC CD4 T cells, naive B cells, and GC B cells. Each spectrum is obviously different, indicating that these spectra could be used as molecular barcodes to identify a particular cell phenotype. Three ions (m/z 715, 747, and 882) with different tissue distribution in the images and found in different relative abundances in each cell phenotype are shown to indicate that these ions may be specific to those cell phenotypes in comparison to the others (this cannot be extrapolated to comparisons of cell phenotypes not investigated in this study). A Venn diagram showing the monoisotopic lipid ions detected in each cell type and their uniqueness and overlap is presented for emphasis that the lipid mass spectra from each cell type are distinguishable from one another.

Comparative lipidomic profiling of tonsillar cell subsets

Access to fresh tonsillar tissues allowed for a comparative lipidomic profiling approach, utilizing specific, flow cytometry sorted CD4$^+$ and B cell subsets for MALDI-TOF mass spectrometry and MSI of sections from the same tissue (Figure S5C). Tonsillar cells were sorted based on known receptors for follicular helper CD4 T cells (T_{FH}) (CD4$^+$CD27$^+$CD45RO + PD1^{hi}CD57^{hi}, a GC enriched T_{FH} subset[20]) and B cells (naive-CD19^{hi}IgD^{hi}, GC enriched-CD19^{hi}CD20^{hi}CD38^{dim}). First, the mass spectra (positive and negative ion mode) for unfractionated tonsillar extracts were generated by MALDI-TOF (Figure 7A). A comparison of the negative ion mode single stage mass spectra acquired for the entire tissue section and the corresponding unfractionated tonsillar extract are shown (Figure 7B). Although more features were observed in the spectrum for extracted tissue compared to the imaging profile, the major features remained the same (e.g., the base peak in all average negative ion mode spectra was m/z 885, the "canonical" phosphatidy-linositol (PI 38:4) ion). Our cell-based lipidomic profiling represents the relative abundance of a given lipid for the entire tissue while its MSI analysis only for the imaged plane which may not always represent the distribution of a lipid across the whole tissue. Positive ion mode spectra comparisons between MS images and cellular extracts were also similar in both features detected and relative abundances; negative ion mode spectra were chosen for display in Figure 7B because of reduced dominance of the PC ion series. These data serve to further confirm MSI results with respect to compounds detected and their relative abundances in the tissue. The averaged mass spectra for three sorted lymphocyte cell subsets and respective images of three ions (m/z 715, m/z 747 and m/z 882) found in those cells and localized to regions where

they are known to reside are shown in Figure 7C. Overlays are also shown to highlight the unique tissue distribution of these ions with respect to the others (Figure 7C). In total, 57, 51, and 48 monoisotopic ions were detected in negative ion mode uniquely in the GC CD4 T cells, naive B cells, and GC B cells, respectively (Figure 7C). 23, 7, and 12 unique monoisotopic ions were putatively identified in each of these cell types, respectively (Table S1). Since we were only comparing these three cell types to each other, this does not necessarily suggest that all these ions are unique to one human cell type. However, it is possible that a subset of these ions could be used for phenotypic characterization complementary to other molecular analysis methods. Our data demonstrate that the complementary application, when access to tissue-derived cells is possible, of mass spectrometry-based cell phenotyping and MSI methodologies could provide meaningful information regarding the lipid spatial localization and cellular origin with high specificity based on the markers used for sorting.

DISCUSSION

Lymphoid follicles are the micro-anatomical sites where B cell maturation and the development of antigen-specific B cell responses occur. The development of these responses is a multi-step process wherein a wide range of innate and adaptive immune cell subsets function in a coordinated mode. Within the GCs, the quality of the T_{FH} "help" received by GC B cells ultimately determines the quality of B cell responses.[27] The different phases of this process are mediated by interactions between immune and non-immune cell subsets and take place in distinct lymphoid tissue areas. This compartmentalization of immune interactions could facilitate (1) the ordered interaction between different immune cell subsets as well as between immune cells and other tissue determinants (e.g., stromal cells FRC, FDCs) and (2) the creation of multi-step checkpoints that could prevent unwanted immune reactions (e.g., autoimmunity, presence of cytotoxic cells like CD8 and NKs in GCs). The relatively easy access, the preservation of distinct anatomical areas, and the presence of numerous mature follicles make tonsil an ideal tissue for the understanding of SLO immune organization. In line with our previous data,[20] we found a high representation of tonsillar T_{FH} subsets (PD-1^{hi}CD57^{lo}, PD-1^{hi}CD57^{hi}), while the majority of CD8 T cells express a naive phenotype, suggesting a limited 'Th1' type immune reactivity in this tissue environment. A balanced representation among different B cell subsets was found, while a significant correlation between GC B cells and T_{FH} subsets, especially the CD57^{hi} ones, or plasma cells was observed. Therefore, the cellular composition determined by flow cytometry points to a coordinated development, possibly supported by mutual regulation[6] of major tonsillar GC cell players and could set the stage for similar comparisons in lymph nodes from diseased subjects. Given the use of tissue-derived cells, flow cytometry provides a relatively robust estimation of cell subset frequencies across the tissue, a measurement that could be used as a reference for the interpretation of quantitative data from imaging analysis when tissue-derived cells are available.

We applied a quantitative multiplex imaging pipeline for the analysis of the spatial organization of major cell subsets in tonsillar areas. A skewed distribution of several cell subsets analyzed was observed among the main tonsillar areas (Extrafollicular, MZ, GC). Our data confirmed the relative absence of CD8 T cells from the GC area, a profile compatible with 'immune privileged' sanctuary areas, where the uncontrolled presence of cellular sources of killing mediators like FasL could be detrimental for the local immune cell subsets (T_{FH}, GC B cells) that overexpress Fas.[28] Similar to flow cytometry data, a significant correlation between T_{FH} and GC B cells was found. Contrary to CD14^{hi} monocytes, a skewed representation of CD68 within the GC and MZ was found, marking the so-called tingible body macrophages.[29] Besides the compartmentalized positioning of cell types, we found a differential expression of secreted mediators like CXCL13 and IL17. Their skewed positioning is compatible with their function (trafficking of T_{FH}, B cells through CXCR5 in the case of CXCL13). The absence of IL17 from the follicular area, particularly GC, is in line with our previous observation that T_{FH} subsets are not capable of secreting this cytokine.[24] We assessed the expression level per cell for CD20, a widely used B cell marker, between different follicular areas. We found a diminished expression in the MZ (IgD^{hi} B cells) while the highest expression was found in the LZ. Therefore, the quantitative imaging data are complementary to flow cytometry generated ones and can facilitate the assignment of specific tissue positioning to B cell phenotypes identified by flow cytometry. This is in line with the recently described positioning of CD57^{lo} and CD57^{hi} T_{FH} cells across the follicular areas.[20] Therefore, the combinational use of these two platforms can significantly increase our capabilities for understanding the tissue immune system organization.

Owing to their fluorescent labeling paradigm, flow cytometry and confocal tissue imaging can provide only 'targeted' data with respect to the molecules/markers under investigation. In addition, these

methodologies cannot provide any information for molecules without a known specific probe (e.g., lipids and metabolites). Lipids are abundant molecules that can mediate a wide range of functions including formation of cellular membranes, signal transduction, and chemo-attraction (e.g., lymphoblast chemo-attraction by human plasma via lysophosphatidylcholine[30]). We applied a mass spectrometry-based imaging platform to access the distribution of several lipids across tonsillar areas. To this end, we performed an untargeted screening MSI protocol using both positive and negative ion modes. Advantages of negative ion mode, when analyzing glycerophospholipids under the conditions described, are (1) the reduced spectral complexity because of ionic adducts and (2) the reduced dominance of PCs in the mass spectrum as compared to positive ion mode. One advantage of positive ion mode lipid imaging is the detection of metal ion adducts from compounds otherwise unionizable by MALDI (e.g., DAGs and TAGs). A limitation to both modes on the instrument used for these analyses is the lower mass resolving power than is required for isotopic fine structure analysis and separation of isobaric species. Often this is required for positive identification of compounds in complex mixtures with no separation before the mass analyzer (Figure S6). Because MSI is performed *in situ*, the only currently available instruments that can separate isobaric ions before the mass analyzer are hybrid ion mobility spectrometer-mass spectrometers. Another commonly employed strategy for positive identification of compounds is to use a higher mass resolving power (but lower throughput) mass spectrometer for MSI experiments; however, this strategy often does not overcome ambiguousness associated with isomers (compounds with the same chemical formula and exact mass).

Previous work on lymphoid tissue lipidomics/metabolomics is sparse. However, human formalin-fixed paraffin embedded (FFPE) tonsils sections have been mapped using time-of-flight secondary ion mass spectrometry (TOF-SIMS), a high lateral resolution MS imaging technique.[16] 189 metabolites in tonsils were found and some of them were associated with T and B lymphocytes in tonsils by using isotope-labeled antibodies such as anti-CD4 and anti-CD20, respectively. The major limitations to TOF-SIMS are its low upper limit of molecular weight ions that can be detected using the commonly employed methods and extensive in-source fragmentation of compounds by the particle beam; therefore, only lipid fragments and other small metabolites were detected in the aforementioned study. MALDI-TOF MS has a much higher high mass cut off in the hundreds of kilodaltons and much less in-source fragmentation, allowing detection and relative quantification of a much more diverse repertoire of compounds. This leads to fewer inferences as to the origins of fragment ions detected. In contrast to the previous study, Yagnik et al.[18] proposed a multiplexed immunohistochemistry (IHC) method based on MALDI imaging to detect immune cells such as helper T cells, cytotoxic T cells, memory T cells and B cells in FFPE tonsil tissue by using a tissue labeling approach with photocleavable isotope-labeled fluorescent antibodies, allowing liberation and detection of mass tags once the laser irradiates the sample. Denti et al. also performed a lipid signature study of T lymphocytes found in FFPE human tonsil tissue by using MALDI-MSI and IHC.[17] They found that glycerophospholipids such as phosphatidic acids (*m/z* 701.5, PA 18:0/18:1; *m/z* 723.4, PA 20:4/18:0; *m/z* 725.4, PA 18:0/18:3) and phosphatidylethanolamine (*m/z* 702.6, PE 40:2) were highly abundant in regions with major presence of T lymphocytes identified by CD3, CD4 and CD8 antibodies but lower in regions containing epithelial cells. These ions were also present in tonsils subjected to our MSI experiments (Figure S7) in tissue regions which could be enriched for several different T cell phenotypes. However, *m/z* 701.5 and 702.6 were the only ions detected in sorted cell lipid extracts and they were both present in both T and B cell subsets. It is possible that differences in tissue localization of all four ions observed in our MSI experiments when compared to the previous study are because of sample processing (i.e., the tonsils used in our study were fresh frozen and the tonsils in the previous study were deparaffinized FFPE). There are many experimental variables that are different between the two studies.

We found a compartmentalized distribution of several lipids analyzed. Using three ions, *m/z* 703, 725 and 728, representing SM 34:1, SM 36:4, and PC 32:3, respectively, we were able to computationally segment the tonsillar epithelia/crypts, extrafollicular, and follicular areas in positive ion mode. In negative ion mode, we were able to produce similar results with enrichment for non-PC lipids and lyso-lipids. There were 24 ions and 20 ions detected in positive ion mode and negative ion mode, respectively, with a more abundant distribution in the follicular areas than in the extrafollicular areas. Unsurprisingly, phosphatidylcholines (PCs, ~ *m/z* 700–800), major constituents of the total membrane mass[31] and essential nutrients required to maintain lymphoid cells in culture,[32] were found to be the most abundant lipid ions detected in positive mode MSI experiments. In fact, PCs are usually so dominant in positive mode MALDI-TOF mass spectra that many other cationizable lipids may be suppressed. In negative ion mode MALDI, both PCs and SMs

lose a methyl (-CH₃) group from the quaternary amine choline moiety, rendering it neutral, and the single negative charge resides on the phosphate moiety. Negative mode tandem mass spectrometry (MS/MS) is able to discriminate PCs from SMs by presence/absence of fatty acyl carboxylate anions in the tandem mass spectrum (i.e., PCs are able to liberate ionizable acyl groups through collisional activation while SMs cannot). Both PCs and SMs are identifiable by a phosphocholine-minus-methyl fragment (*m/z* 168), a phosphate ion (*m/z* 79), and a phosphonate ion (*m/z* 97) in the tandem mass spectrum. Unlike PCs, increased membrane PIs impart net negative charge to the cellular membrane which affects membrane fluidity, shape, and the types of other non-PI components found in PI-rich membrane loci.[33] They are observed in negative ion mode as singly deprotonated ions with high sensitivity. This is an advantage to using negative ion mode for PI analysis since PIs have no proton acceptor groups; they are detected in positive mode, if at all, as cation adducts which requires further spectral interpretation. PIs are also the precursors of phosphoinositides, kinase-phosphorylated PIs that are important mediators of many G protein-coupled receptor (GPCR) reactions in the cytosol.[34] A PI at *m/z* 882 (likely an isotopic peak with less isobaric interference than its respective monoisotopic peak), confirmed by MS/MS and found to be selectively expressed in GCs, was also found in sorted GC B cells. Furthermore, the pattern was not homogeneous across the follicular area, indicating that this lipid could be differentially expressed in the GC subareas LZ and DZ. Co-registration experiments using antibodies against protein biomarkers expressed in these areas would be highly informative in this regard. It is possible that GC cells use this PI, or a suite of PIs with similar acyl chain characteristics, for modification and signaling through phosphoinositides. Alternatively, GC B cells, a cellular pool characterized by excessive proliferation, may produce an abundant and/or diverse pool of PIs as cellular mediators to accommodate relevant proliferation signaling.[35] Finally, GC cells may simply increase their PI repertoire to facilitate physical phenotypic changes. Sorted tissue-derived cells demonstrated unique subsets of the similar MSI and extracted whole tonsil lipidomes, further confirming our hypothesis that these cells can be differentiated by their unique lipid signatures serving as molecular 'barcodes'.

An in-house pipeline for multimodal tissue imaging was developed and implemented to correlate molecular and cell phenotype marker images with tissue compartments. Several multimodal approaches have focused on imaging serial tissue sections with complementary imaging modalities. However, Dewez et al.[36] and Patterson et al.[37] have used tissue craters, created by laser desorption in MSI, as teaching points to co-register laser capture microdissection (LCM) microscopy or fluorescence microscopy with MSI images, respectively. One notable advantage to the analysis of serial sections is that multiple analyses can be performed in parallel, increasing sample throughput. However, one advantage of multimodal analysis of the same tissue section is that it drastically decreases the difficulty in co-registering complementary images either by image coordinates or experimental metadata. Another advantage is that the signal from each imaging modality can be inferred as coming from the same cells and extracellular components within the tissue. In our approach, we used an already available tool in the data analysis software to reliably co-register images from multispectral scanning confocal microscopy and lipid MSI. Once these images are co-registered, the files can be saved and mined as new experimental hypotheses arise, thus enabling creation of a multimodal databank in our laboratory. These data in combination with banked lymphocyte lipidomics data will increase our confidence in assigning specific molecular components with cell phenotypes observed in a confocal image. Although our image co-registration approach could benefit from more sophisticated alignment algorithms, the approach used in this study is sufficient to observe ions colocalized to specific tissue segments known to be highly enriched for certain cell phenotypes.

Our data demonstrate a compartmentalization of the human lymphoid organ immune system at different levels including cells, lipids, and secreted protein factors. In line with previously described data,[20] this anatomical compartmentalization most likely reflects functional compartmentalization too. We propose an experimental approach of complementary methodologies that can provide unpresented information regarding biological factors contributing to this tissue spatial organization of the immune system. A multimodal tissue analysis integrating the high resolution and volumetric (z axis) analysis of scanning confocal imaging combined with the high throughput and data-rich performance of modern MSI, especially for targets with no known probes, can lead to discovery of novel biomolecules with potential roles for the described immune system anatomy. Furthermore, the current study could serve as a reference for future studies comparing the tissue organization of the human immune system between health and disease.

Limitations of the study

The current study and workflow development will be used to delineate the lymphoid organ immune land-scaping at multiple levels in future studies. However, some of the lipid ions indicative of tonsillar anatomy may not directly translate to other secondary lymphoid tissues such as lymph nodes and spleen. This will require further validation of the method in other tissues. Unambiguous identifications of lipid ions also require more specific analytical approaches or complementary techniques. In addition, the multimodal imaging pipeline described likely will not be applicable to all fluorescent antibodies used widely for confocal imaging. In some cases, UV-absorbing chemical matrices used for MALDI imaging could interfere with fluorescence signals in the subsequent step. These limitations will be empirically determined as needed in further studies. Finally, comparisons between cell lipidomes in flow cytometry-sorted cells and cells residing in tissues *in situ* are not well understood. These similarities and differences require further exploration.

STAR★METHODS

Detailed methods are provided in the online version of this paper and include the following:

- KEY RESOURCES TABLE
- RESOURCE AVAILABILITY
  - Lead contact
  - Materials availability
  - Data and code availability
- METHOD DETAILS
  - Experimental model and study participant details
  - Flow cytometry studies
  - Immunofluorescence microscopy studies
  - MALDI-TOF mass spectrometry imaging (MSI) studies
- QUANTIFICATION AND STATISTICAL ANALYSIS

SUPPLEMENTAL INFORMATION

Supplemental information can be found online at https://doi.org/10.1016/j.isci.2023.107261.

AUTHOR CONTRIBUTIONS

B.L.O.: Conceptualization, Data curation, Formal Analysis, Investigation, Methodology, Project administration, Visualization, Writing- original draft, Writing-review and editing; J.A.V-D.: Formal Analysis, Investigation, Methodology, Writing-original draft, Writing-review and editing; E.M., A.M., K.M., and G.F.: Formal Analysis, Investigation, Methodology, Visualization, Writing-review and editing; K.I.: formal analysis, investigation; D.A.: Investigation, Methodology, Visualization, Writing-review and editing; L.D.L.: Methodology, Resources; A.S.W: Methodology, Resources, Writing- original draft, Writing-review and editing; R.A.K.: Funding acquisition, Project administration, Resources, Supervision, Writing-review and editing; CP: Conceptualization, Data curation, Formal Analysis, Funding acquisition, Methodology, Project administration, Resources, Supervision, Visualization, Writing- original draft, Writing-review and editing.

DECLARATION OF INTERESTS

The authors have no conflict of interest to declare.

REFERENCES

1. Turk, J.L. (1977). The organization of lymphoid tissue in relation to function. Lymphology 10, 46–53.

2. Kumar, B.V., Connors, T.J., and Farber, D.L. (2018). Human T cell development, localization, and function throughout Life. Immunity 48, 202–213. https://doi.org/10.1016/j.immuni.2018.01.007.

3. Trepel, F. (1974). Number and distribution of lymphocytes in man. A critical analysis. Klin. Wochenschr. 52, 511–515. https://doi.org/10.1007/BF01468720.

4. Uhlén, M., Fagerberg, L., Hallström, B.M., Lindskog, C., Oksvold, P., Mardinoglu, A., Sivertsson, Å., Kampf, C., Sjöstedt, E., Asplund, A., et al. (2015). Proteomics. Tissue-based map of the human proteome. Science 347, 1260419. https://doi.org/10.1126/science.1260419.

5. Luscieti, P., Hubschmid, T., Cottier, H., Hess, M.W., and Sobin, L.H. (1980). Human lymph node morphology as a function of age and site. J. Clin. Pathol. 33, 454–461. https://doi.org/10.1136/jcp.33.5.454.

6. Baumjohann, D., Preite, S., Reboldi, A., Ronchi, F., Ansel, K.M., Lanzavecchia, A., and Sallusto, F. (2013). Persistent antigen and germinal center B cells sustain T follicular helper cell responses and phenotype. Immunity 38, 596–605. https://doi.org/10.1016/j.immuni.2012.11.020.

7. Lanzavecchia, A., and Sallusto, F. (2001). Regulation of T cell immunity by dendritic cells. Cell 106, 263–266. https://doi.org/10.1016/s0092-8674(01)00455-x.

8. Goodnow, C.C., Vinuesa, C.G., Randall, K.L., Mackay, F., and Brink, R. (2010). Control systems and decision making for antibody production. Nat. Immunol. 11, 681–688. https://doi.org/10.1038/ni.1900.

9. McHeyzer-Williams, M., Okitsu, S., Wang, N., and McHeyzer-Williams, L. (2011). Molecular programming of B cell memory. Nat. Rev. Immunol. 12, 24–34. https://doi.org/10.1038/nri3128.

10. Lanzavecchia, A. (1985). Antigen-specific interaction between T and B cells. Nature 314, 537–539. https://doi.org/10.1038/314537a0.

11. Röhlich, K. (1930). Beitrag zur Cytologie der Keimzentren der Lymphknoten. Z. Mikrosk. Anat. Forsch. (Leipz.) 20, 287–297.

12. Qin, D., Wu, J., Vora, K.A., Ravetch, J.V., Szakal, A.K., Manser, T., and Tew, J.G. (2000). Fc gamma receptor IIB on follicular dendritic cells regulates the B cell recall response. J. Immunol. 164, 6268–6275. https://doi.org/10.4049/jimmunol.164.12.6268.

13. Balogh, P., Aydar, Y., Tew, J.G., and Szakal, A.K. (2002). Appearance and phenotype of murine follicular dendritic cells expressing VCAM-1. Anat. Rec. 268, 160–168. https://doi.org/10.1002/ar.10148.

14. Wang, Y., and Carter, R.H. (2005). CD19 regulates B cell maturation, proliferation, and positive selection in the FDC zone of murine splenic germinal centers. Immunity 22, 749–761. https://doi.org/10.1016/j.immuni.2005.04.012.

15. Gatto, D., and Brink, R. (2010). The germinal center reaction. J. Allergy Clin. Immunol. 126, 898–907. quiz 908-9; quiz 908-899. https://doi.org/10.1016/j.jaci.2010.09.007.

16. Ganesh, S., Hu, T., Woods, E., Allam, M., Cai, S., Henderson, W., and Coskun, A.F. (2021). Spatially resolved 3D metabolomic profiling in tissues. Sci. Adv. 7, eabd0957. https://doi.org/10.1126/sciadv.abd0957.

17. Denti, V., Mahajneh, A., Capitoli, G., Clerici, F., Piga, I., Pagani, L., Chinello, C., Bolognesi, M.M., Paglia, G., Galimberti, S., et al. (2021). Lipidomic typing of colorectal cancer tissue containing tumour-infiltrating lymphocytes by MALDI mass spectrometry imaging. Metabolites 11, 599. https://doi.org/10.3390/metabo11090599.

18. Yagnik, G., Liu, Z., Rothschild, K.J., and Lim, M.J. (2021). Highly multiplexed immunohistochemical MALDI-MS imaging of biomarkers in tissues. J. Am. Soc. Mass Spectrom. 32, 977–988. https://doi.org/10.1021/jasms.0c00473.

19. Moysi, E., Del Rio Estrada, P.M., Torres-Ruiz, F., Reyes-Terán, G., Koup, R.A., and Petrovas, C. (2021). In situ characterization of human lymphoid tissue immune cells by multispectral confocal imaging and quantitative image analysis; implications for HIV reservoir characterization. Front. Immunol. 12, 683396. https://doi.org/10.3389/fimmu.2021.683396.

20. Padhan, K., Moysi, E., Noto, A., Chassiakos, A., Ghneim, K., Perra, M.M., Shah, S., Papaioannou, V., Fabozzi, G., Ambrozak, D.R., et al. (2021). Acquisition of optimal TFH cell function is defined by specific molecular, positional, and TCR dynamic signatures. Proc. Natl. Acad. Sci. USA 118, e2016855118. https://doi.org/10.1073/pnas.2016855118.

21. Amodio, D., Cotugno, N., Macchiarulo, G., Rocca, S., Dimopoulos, Y., Castrucci, M.R., De Vito, R., Tucci, F.M., McDermott, A.B., Narpala, S., et al. (2018). Quantitative multiplexed imaging analysis reveals a strong association between immunogen-specific B cell responses and tonsillar germinal center immune dynamics in children after influenza vaccination. J. Immunol. 200, 538–550. https://doi.org/10.4049/jimmunol.1701312.

22. Petrovas, C., Ferrando-Martinez, S., Gerner, M.Y., Casazza, J.P., Pegu, A., Deleage, C., Cooper, A., Hataye, J., Andrews, S., Ambrozak, D., et al. (2017). Follicular CD8 T cells accumulate in HIV infection and can kill infected cells in vitro via bispecific antibodies. Sci. Transl. Med. 9, eaag2285. https://doi.org/10.1126/scitranslmed.aag2285.

23. Kroenke, M.A., Eto, D., Locci, M., Cho, M., Davidson, T., Haddad, E.K., and Crotty, S. (2012). Bcl6 and Maf cooperate to instruct human follicular helper CD4 T cell differentiation. J. Immunol. 188, 3734–3744. https://doi.org/10.4049/jimmunol.1103246.

24. Petrovas, C., Yamamoto, T., Gerner, M.Y., Boswell, K.L., Wloka, K., Smith, E.C., Ambrozak, D.R., Sandler, N.G., Timmer, K.J., Sun, X., et al. (2012). CD4 T follicular helper cell dynamics during SIV infection. J. Clin. Invest. 122, 3281–3294. https://doi.org/10.1172/JCI63039.

25. Wymann, M.P., and Schneiter, R. (2008). Lipid signalling in disease. Nat. Rev. Mol. Cell Biol. 9, 162–176. https://doi.org/10.1038/nrm2335.

26. McLafferty, F.W., and Tureccek, F.E. (1993). Interpretation of Mass Spectra, 4th Edition (University Science Books).

27. Victora, G.D., and Nussenzweig, M.C. (2022). Germinal Centers. Annu. Rev. Immunol. 40, 413–442. https://doi.org/10.1146/annurev-immunol-120419-022408.

28. Lagresle, C., Bella, C., Daniel, P.T., Krammer, P.H., and Defrance, T. (1995). Regulation of germinal center B cell differentiation. Role of the human APO-1/Fas (CD95) molecule. J. Immunol. 154, 5746–5756.

29. Park, S.M., Brooks, A.E., Chen, C.J.J., Sheppard, H.M., Loef, E.J., McIntosh, J.D., Angel, C.E., Mansell, C.J., Bartlett, A., Cebon, J., et al. (2021). Migratory cues controlling B-lymphocyte trafficking in human lymph nodes. Immunol. Cell Biol. 99, 49–64. https://doi.org/10.1111/imcb.12386.

30. Hoffman, R.D., Kligerman, M., Sundt, T.M., Anderson, N.D., and Shin, H.S. (1982). Stereospecific chemoattraction of lymphoblastic cells by gradients of lysophosphatidylcholine. Proc. Natl. Acad. Sci. USA 79, 3285–3289. https://doi.org/10.1073/pnas.79.10.3285.

31. Ridgway, N.D. (2018). How CCTalpha puts a leash on phospholipid synthesis. J. Biol. Chem. 293, 7085–7086. https://doi.org/10.1074/jbc.H118.002882.

32. Cui, Z., and Houweling, M. (2002). Phosphatidylcholine and cell death. Biochim. Biophys. Acta 1585, 87–96. https://doi.org/10.1016/s1388-1981(02)00328-1.

33. Pöyry, S., and Vattulainen, I. (2016). Role of charged lipids in membrane structures - Insight given by simulations. Biochim. Biophys. Acta 1858, 2322–2333. https://doi.org/10.1016/j.bbamem.2016.03.016.

34. de Rubio, R.G., Ransom, R.F., Malik, S., Yule, D.I., Anantharam, A., and Smrcka, A.V. (2018). Phosphatidylinositol 4-phosphate is a major source of GPCR-stimulated phosphoinositide production. Sci. Signal. 11, eaan1210. https://doi.org/10.1126/scisignal.aan1210.

35. Herzog, S., Reth, M., and Jumaa, H. (2009). Regulation of B-cell proliferation and differentiation by pre-B-cell receptor signalling. Nat. Rev. Immunol. 9, 195–205. https://doi.org/10.1038/nri2491.

36. Dewez, F., Martin-Lorenzo, M., Herfs, M., Baiwir, D., Mazzucchelli, G., De Pauw, E.,

Heeren, R.M.A., and Balluff, B. (2019). Precise co-registration of mass spectrometry imaging, histology, and laser microdissection-based omics. Anal. Bioanal. Chem. *411*, 5647–5653. https://doi.org/10.1007/s00216-019-01983-z.

37. Patterson, N.H., Tuck, M., Van de Plas, R., and Caprioli, R.M. (2018). Advanced registration and analysis of MALDI imaging mass spectrometry measurements through autofluorescence microscopy. Anal. Chem. *90*, 12395–12403. https://doi.org/10.1021/acs.analchem.8b02884.

38. Ioannidou, K., Ndiaye, D.R., Noto, A., Fenwick, C., Fortis, S.P., Pantaleo, G., Petrovas, C., and de Leval, L. (2020). In situ characterization of follicular helper CD4 T cells using multiplexed imaging. Front. Immunol. *11*, 607626. https://doi.org/10.3389/fimmu.2020.607626.

39. Kolářová, L., Prokeš, L., Kučera, L., Hampl, A., Peña-Méndez, E., Vaňhara, P., and Havel, J. (2017). Clusters of monoisotopic elements for calibration in (TOF) mass spectrometry. J. Am. Soc. Mass Spectrom. *28*, 419–427. https://doi.org/10.1007/s13361-016-1567-x.

STAR★METHODS

KEY RESOURCES TABLE

REAGENT or RESOURCE	SOURCE	IDENTIFIER
Antibodies		
CD3-H7APC	BD Biosciences	SK7; 560176; RRID: AB_1645475
CD4-BV650	BD Biosciences	SK3; 563875; RRID: AB_2744425
CD8-Pacific Blue	BD Biosciences	RPA-T8; 558207; RRID: AB_397058
CD19-FITC	Beckman Coulter	J3-119; IM1284U; RRID: AB_131011
CD27-BV605	BioLegend	O323; 302830; RRID: AB_2561450
CD45RO-Cy5PE	BD Biosciences	UCHL1; 555494; RRID: AB_395885
PD-1-BV711	BioLegend	EH12.2H7; 329928; RRID: AB_2562911
CD57-AF594	Novus Biologicals	NK-1; NBP2-44352
IgD-PE	SouthernBiotech	PE; 2030-09; RRID: AB_2795630
CD20-BV570	BioLegend	2H7; 302332; RRID: AB_2563805
CD38-BV786	BioLegend	HIT2; 303530; RRID: AB_2565893
Recombinant Anti-IgD antibody	Abcam	EPR6146; ab124795; RRID: AB_10974228
CD8 Monoclonal Antibody	Invitrogen	4B11; MA1-80231
Monoclonal mouse anti-human CD68	Agilent	KP1; GA60961-2; RRID: AB_2661840
CD20 Monoclonal Antibody	eBioscience	L26; 42020282
Alexa Fluor 647 Mouse anti-Ki-67	BD Biosciences	B56; 558615; RRID: AB_647130
CD4-AF700	R&D Systems	polyclonal; FAB8165N-100
PD-1-AF488	R&D Systems	polyclonal; FAB7115G; RRID: AB_10973668
CD57-BV480	BD Horizon	NK-1; custom
JoPro	Life Technologies	nuclear stain; discontinued
CD14 rabbit monoclonal antibody	Cell Marque	EPR3653; 114R-16; RRID: AB_2827391
FDC monoclonal antibody	eBioscience	CNA.42; 14-9968-82
CXCL13 rabbit polyclonal antibody	Invitrogen	polyclonal; PA5-28827
Human IL-17/IL-17A antibody	R&D Systems	polyclonal; AF-317-NA; RRID: AB_354463
Chemicals, peptides, and recombinant proteins		
2,5-dihydroxybenzoic acid	Alfa Aesar	J67622
1,5-diaminonaphthalene	Sigma Aldrich	56451
nanoXact 60 nm gold nanospheres	nanoComposix	AGCN60-50M
9-aminoacridine	Sigma Aldrich	92817
Software and algorithms		
FlexAnalysis	Bruker	ver. 3.4
SCiLS Lab Pro	Bruker	ver. 2020a
OriginPro	OriginLab	ver. 2021b
Imaris	Oxford Instruments	ver. 9.6
FlowJo	BD	ver. 10.6.1

RESOURCE AVAILABILITY

Lead contact

Further information and requests for resources and reagents should be directed to and will be fulfilled by the lead contact, Constantinos Petrovas (Konstantinos.Petrovas@chuv.ch)

Materials availability

This study did not generate new unique reagents.

Data and code availability

- All data reported in this paper will be shared by the lead contact upon request.
- This paper does not report original code.
- Any additional information required to reanalyze the data reported in this paper is available from the lead contact upon request.

METHOD DETAILS

Experimental model and study participant details

Fresh tonsils were anonymized discarded pathologic specimens obtained from Children's National Medical Center (CNMC) under the auspices of the Basic Science Core of the District of Columbia Developmental Center for AIDS Research. Anonymized FFPE tissues from two tonsils were obtained from the Institute of Pathology in Lausanne and used for light microscopy imaging studies. The CNMC Institutional Review Board determined that study of anonymized discarded tissues did not constitute 'human subjects research'. Upon receipt, tissues were washed with ice-cold medium R-10 (RPMI 1640 supplemented with 10% fetal bovine serum, 2 mM L-glutamine, 100 U/mL penicillin and 100 μg/mL streptomycin, Invitrogen). Following the removal of surrounding fatty tissue and necrotic areas, part of the tissue was dedicated for fixation (formalin) and paraffin embedded block or snap frozen block preparation while the remaining tissue was cut into small pieces for cell preparation by mechanical disruption, followed by Ficoll-Paque density gradient centrifugation. Cells were stored in liquid nitrogen until further use.

Flow cytometry studies

The following titrated, conjugated antibodies were used for flow cytometry analysis: CD3-H7APC (SK7, BD Biosciences), CD4-BV650 (SK3, BD Biosciences), CD8-Pacific Blue (RPA-T8, BD Pharmingen), CD19-FITC (J3-119, Beckman-Coulter), CD27-BV605 (O323, Biolegend), CD45RO-Cy5PE (UCHL1, BD Pharmingen), PD-1-BV711 (EH12.2H7, Biolegend), CD57-AF594 (NK-1, Novus Bio), IgD-PE (Goat polyclonal, Southern Biotech), CD20-BV570 (2H7, Biolegend), CD38-BV786 (HIT2, Biolegend). 1-2×10^6 tonsil-derived cells were thawed and rested for 2h in a cell culture incubator before staining. Cells were washed with PBS, BSA (0.5%), incubated (5 min, RT) with a viability dye (Aqua-dye, Invitrogen) and surface stained with titrated amounts of antibodies for 30 min at room temperature. After washing, cells were resuspended and fixed with 1% paraformaldehyde.

Data acquisition and analysis

0.5-1 × 10^6 events were collected on a BD LSR Fortessa X-50 flow cytometer (BD Immunocytometry Systems). Electronic compensation was performed with antibody capture beads (BD Biosciences). Data were analyzed using FlowJo Version 9.9.4 (Tree Star). Forward scatter area vs. forward scatter height was used to gate out cell aggregates.

Immunofluorescence microscopy studies

Confocal microscopy imaging

FFPE tissue sections of 8 μm were prepared using a microtome (Leica) and processed (heat drying, deparaffinization) for antigen retrieval (Borg RTU, Biocare Medical) and antibody staining using titrated antibodies as recently described.[19,22] The following combination of antibodies was used: IgD (primary rabbit, clone EPR6146, abcam), CD8 (primary mouse IgG2b, clone 4B11, Invitrogen), CD68 (primary mouse IgG1, clone KP-1, DAKO), CD20-eF615 (clone L26, eBioscience), Ki67-AF647 (clone B56, BD Horizon), CD4-AF700 (goat polyclonal, R&D), PD-1-AF488 (goat polyclonal, R&D), CD57-BV480 (clone NK1, BD Horizon), and JoJo (nuclear marker, Life Technologies). The following titrated secondary antibodies were used: donkey anti-rabbit Brilliant Violet 421 (poly 4064 Biolegend), goat anti-mouse IgG2b Alexa Fluor 546 (A21143, Thermo Scientific) and goat anti-mouse IgG1 Alexa Fluor 546 (A-21123, Thermo Scientific).

Data acquisition and analysis.

Stained slides were imaged on a NIKON (A1) inverted confocal microscope system, equipped with 40X, 1.3 NA oil objective lens. Tissue sections stained with single

fluorophores were used for the correction of the spectral spillover between channels through live spectral unmixing in NIS software. Image acquisition was performed with NIS-elements software and the data analyzed with Imaris software version 9.6 (Bitplane). Histocytometry analysis was performed as previously described.[22] Briefly, imaging datasets were segmented post-acquisition based on nuclear staining and average voxel intensities for all channels were extrapolated in Imaris. Channel statistics were exported to csv (comma separated values) files format and analyzed in FlowJo version 10.6.1.

Multispectral imaging

FFPE tissue sections of 4 μm were cut and prepared for immunofluorescence staining using the following combination of antibodies against CD14 (clone EPR3653, Cell Marque, detection by Opal 570), FDC (clone CNA.42, Invitrogen, detection with Opal 690), CXCL-13 (rabbit polyclonal, ThermoFisher, detection with Opal 520), IL-17 (goat polyclonal, R&D systems, detection with Opal 620), CD20 (clone L26, ThermoFisher, detection with Opal 480) and DAPI (nuclear marker), as previously described.[38] Briefly, the staining consisted of consecutive rounds of antigen retrieval, staining with primary antibody, secondary HRP-labeled antibody and detection with optimized fluorescent Opal tyramide signal amplification (TSA) dye (Opal 7-color Automation IHC kit, from Akoya, Ref. NEL821001KT) and repeated antibody denaturation cycles. Multispectral images were acquired using the latest Vectra Polaris imaging system from Akoya. All images were recorded using a 20× magnification. The Phenochart 1.0.12 software (Akoya), a whole-slide contextual viewer was used for identification of regions of interest and acquisition of unmixed multispectral images.

MALDI-TOF mass spectrometry imaging (MSI) studies

Tissue processing for MSI

Fresh human tonsils were snap frozen in liquid nitrogen following excision as described above. Tissue sections of 10 μm thickness were prepared using an HM525 NX cryostat (Thermo Scientific, Waltham, MA) operated at $-20°C$, and thaw-mounted onto the conductive side of indium tin oxide (ITO)-coated slides. Slides were placed in a vacuum desiccator at -10 mmHg for at least 15 min before matrix deposition. Matrix deposition was performed with a TM-Sprayer (HTX Technologies, Chapel Hill, NC). For positive mode mass spectrometry imaging (MSI) experiments, 2,5-dihydroxybenzoic acid (DHB; Alfa Aesar, Ward Hill, MA) was sprayed onto the glass slide after tissue mounting at a concentration of 30 mg mL^{-1} with 12 passes/cycles (approx. density = 0.001667 mg/mm^2). For negative mode MSI, 1,5-diaminonaphthalene (DAN; Sigma-Aldrich, Burlington, MA) was sprayed onto the glass slide after tissue mounting at a concentration of 5 mg mL^{-1} with 8 passes/cycles (approx. density = 0.009600 mg/mm^2). Universal sprayer settings were as follows: nebulization gas pressure = 10 psi, track spacing = 3 mm, velocity = 1200 mm min^{-1}, CC pattern.

Data acquisition and analysis

Data acquisition was carried out using a rapifleX MALDI TissueTyper tandem time-of-flight (TOF/TOF) mass spectrometer operated at 20 μm lateral resolution (Bruker Daltonics, Billerica, MA). In positive ion mode, 200 laser shots were acquired per pixel with an arbitrary laser power of 39%. In negative ion mode, 300 laser shots were acquired per pixel with an arbitrary laser power of 26%. In both modes, the laser attenuator was set with an offset of 0% and a range of 30%, and the laser repetition rate was 10 kHz. Bare citrate gold nanospheres (nanoXact 60 nm, nanoComposix, San Diego, CA) were used for mass axis calibration in MSI experiments in a similar fashion to that described by Kolarova et al.[39] A mixture of phosphatidylcholines with known exact monoisotopic masses, created in-house, was used for mass axis calibration of lipid extract mass spectra. Acquired data were processed in FlexImaging 5.0 (Bruker Daltonics, Billerica, MA) and SCiLS Lab Pro 2020a (Bruker, Bremen, Germany). Putative lipid identifications were made using a combination of precursor ion *m/z* database searching (LMSD, lipidmaps.org) and *de novo* TOF/TOF product ion assignments. Mass spectra were adapted for size and clarity by regenerating figures using x- and y-coordinates exported from FlexAnalysis ver. 3.4 (Bruker Daltonics, Billerica, MA) and imported into OriginPro ver. 2021b (OriginLab Corporation, Northampton, MA). All mass spectra were normalized to the base peak. Peak picking was performed using the proprietary algorithm (SNAP) in FlexAnalysis ver. 3.4. Deisotoping was performed simultaneously within the same algorithm. Peak lists were generated for monoisotopic ions with signal-to-noise ratio greater than or equal to 2:1. A Venn diagram indicating peak list overlap between different sorted cell types was created using a free online tool from Ghent University Bioinformatics and Evolutionary Genomics laboratory (http://bioinformatics.psb.ugent.be/webtools/Venn).

Multi-modal imaging

Tonsil sections of 8 μm thickness were thaw mounted as described in the previous MSI experimental section onto poly-L-lysine and ITO-coated slides. Negative ion mode lipid images were acquired at 20 μm lateral resolution, also as described previously, with DAN matrix. Following MSI, tissues sections were washed in ethanol (100% for 2 min) to remove the MSI matrix and then rehydrated by washes in decreasing ethanol concentrations (95%, 80%, 70%). Tissue sections were then fixed in 1% paraformaldehyde. Permeabilization for 1 h with a 0.3% Tritox-100 in PBS solution followed. Next, tissues were blocked with 10% goat serum (1 h at RT) and then titrated with conjugated antibodies (2 h at RT). Nuclear staining (JOJO-1, Life Technologies) was applied for 20 min at RT and slides were mounted with with Fluoromount-G (Southern Biotech). Confocal imaging was performed as described in the previous section. Since the same tissue section was used for both MSI and confocal microscopy experiments, the image co-registration was relatively simple and could be perfomed using the "co-register image" wizard in FlexAnalysis after importing.tif files of confocal images generated in Imaris.

Lymphocyte sorting and preparation for MALDI-TOF MS

Cells from two human tonsils were labeled and sorted as previously described.[20] Briefly, $PD1^{hi}CD57^{hi}$ follicular helper CD4 T cells (T_{FH}), $CD19^{hi}IgD^{hi}$ (naive) and $CD19^{hi}IgD^{low}CD20^{hi}CD38^{dim}$ (enriched in germinal center-GC) B cells were sorted. The $PD1^{hi}CD57^{hi}$ tonsillar T_{FH} subset was chosen given its exclusive localization within the GC borders.[20] Following sorting, cells were suspended in Mg^{2+} and Ca^{2+} -free phosphate buffered saline (PBS, pH 7.4), flash frozen, and stored at −80°C until further analysis.

Lipid extraction and analysis from tonsil tissue and sorted cells

Small pieces (∼1 mg) of snap-frozen human tonsils were dissected from the intact specimen and homogenized in 400 μL of deionized water (11.2 MΩ, 4°C) followed by the addition of 800 μL of LC/MS grade chloroform/methanol (1:2 v/v). Sorted B and T lymphocytes were similarly treated. The resulting mixture was vortexed (2500 rpm, 2 min), sonicated for 2 min and subsequently incubated on dry ice for 10 min. Next, 300 μL of LC/MS grade chloroform/water (43:57% v/v) was added and the final mixture was also vortexed (2500 rpm, 2 min) and sonicated for 2 min, then centrifuged (3000 rpm for 5 min at 4°C) and the lower organic phase containing lipids dissolved in chloroform collected and kept at −80°C. The remaining upper phase and precipitate were collected for lipids re-extraction by adding 500 μL of chloroform/methanol (1:2 v/v). This mixture was vortexed (2500 rpm, 2 min), sonicated (2 min) and incubated on dry ice for 10 min. Subsequently, it was centrifuged (3000 rpm for 5 min at 4°C) and the lower phase collected and added to the first lipid extract. The total extract was stored at −80°C prior to MS analysis. 10 mM stock solutions of DHB and 9-aminoacridine (9-AA) MALDI matrices in methanol were used for MALDI MS analysis of extracted lipids in positive and negative ion modes, respectively. 10 μL of each matrix solution was individually mixed with an equal volume of the lipid extracts (from either tonsil tissue or lymphocytes). The lipid/matrix solutions were vortexed for 3 min at 2500 rpm and 2 μL of the final solution was deposited on a MALDI AnchorChip target plate allowing the spots to co-crystallize at room temperature prior to MS analysis. 9-AA was used for negative mode extracts assay and gave better co-crystallization for spotted samples than previously observed with DAN.

QUANTIFICATION AND STATISTICAL ANALYSIS

Flow cytometry and histocytometry generated data were analyzed using linear regression and the Wilcoxon and Kruskal-Wallis tests. Statistical analysis was performed with Prism software (version 6; GraphPad Software, La Jolla, California). Results were considered to be significant when $p < 0.05$. For MSI data, probabilistic latent semantic analysis (pLSA) was used to build a model with 5 components to differentiate the tonsillar follicle from the extrafollicular space. This was performed in SCiLS Lab Pro pLSA module. Box and whiskers plots for ions of interest with higher observed intensities in the segment defined as the follicle than in other tissue segments were also generated in SCiLS Lab Pro. Comparison of median intensity values was performed using a Kruskal-Wallis test.